

Unveiling Molecular Moieties through Hierarchical Graph Explainability

Paolo Sortino^{1,‡}, Salvatore Contino^{1,*‡}, Ugo Perricone^{2,*}, Roberto Pirrone¹

March 1, 2024

Abstract

Background: Graph Neural Networks (GNN) have emerged in very recent years as a powerful tool for supporting *in silico* Virtual Screening. In this work we present a GNN which uses Graph Convolutional (GC) architectures to achieve very accurate multi-target screening. We also devised a hierarchical Explainable Artificial Intelligence (XAI) technique to catch information directly at atom, ring, and whole molecule level by leveraging the message passing mechanism. In this way, we find the most relevant moieties involved in bioactivity prediction.

Results: We report a state-of-the-art GNN classifier on twenty Cyclin-dependent Kinase targets in support of VS. Our classifier outperforms previous SOTA approaches proposed by the authors. Moreover, a CDK1-only high-sensitivity version of the GNN has been designed to use our explainer in order to avoid the inherent bias of multi-class models. The hierarchical explainer has been validated by an expert chemist on 19 approved drugs on CDK1. Our explainer provided information in accordance to the docking analysis for 17 out of the 19 test drugs.

Conclusion: Our approach is a valid support for shortening both the screening and the hit-to-lead phase. Detailed knowledge about the molecular substructures that play a role in the inhibitory action, can help the computational chemist to gain insights into the pharmacophoric function of the molecule also for repurposing tasks.

1 Background

The development of a new drug is a long and time-consuming process that, despite advances in technology and computer applications, is fragmented into several steps before being able to identify a lead compound that can be tested on *in vivo* models. Over the last decade, the use of deep learning has provided support to the Virtual Screening (VS) campaigns for the efficient selection of hit compounds by strengthening predictions through the use of massive data in the training model phase [11, 4, 22, 3, 29]. Indeed, being able to correctly prioritise active molecules during the screening steps speeds up the discovery process. Classical approaches used in Computer Aided Drug Design (CADD) are not always efficient, being affected by the

*corresponding author salvatore.contino01@unipa.it (Salvatore Contino), uperricone@fondazionerimed.com (Ugo Perricone)

‡These authors contributes equally.

¹Department of Engineering, University of Palermo, 90128 Palermo, Italy

²Molecular Informatics Group, Fondazione Ri.MED, 90128 Palermo, Italy

use of specific force field [21, 13] and the quality of structural data available, thus affecting the hit optimisation steps towards the lead compound. Hit discovery is the very first step after screening, and chemists use it as the starting point to optimise hits rationally until designing a lead compound. This step uses different techniques such as hit expansion, (bio)isosteric replacement or a combination of them [10]. Hit expansion, for instance, is one of the most widely used techniques for optimisation and it is based on the synthesis of analogues to the selected small molecule by replacing chemical patterns, guided by data obtained from Structure Activity Relationship (SAR) analysis [2]. (Bio)isosteric replacement is a technique based on the definition of isosterism introduced by Langmuir in 1919, during his studies of the physico-chemical properties of atoms and chemical groups. He noted that atoms with similar properties trigger the same biological effect; for example, compounds with the same number of atoms and electrons (e.g. N₂, CO, N₂O, etc.) are isosteric and trigger the same biological behaviour. On the basis of the same electron arrays, the chemical groups have been divided into 21 groups that are used to optimise bioactive molecules by increasing their efficiency as [7] drugs. Clearly, optimisation requires an understanding of the relevant atoms or chemical groups within the small molecule. This step is usually handled by the computational chemist, who recognizes and consciously acts to improve the molecule’s activity in accordance with their knowledge and expertise in the field.

In this context, Graph Neural Networks (GNN) [18, 12] have emerged as powerful tools in Drug Discovery and Virtual Screening due to their ability to model complex molecular structures and interactions. By leveraging the graph-based representation of molecules to capture local and global structural information, GNNs offer a promising approach for predicting molecular properties, bioactivity and drug-target interactions [9, 28, 24, 26, 20, 5, 23].

In the present work, we are presenting a GNN based on the so called Graph Convolutional layers, which firstly prioritise molecules towards a set of 20 kinases with a very high rate of precision, and also supports the computational chemist in the selection of the most important chemical features in the host-guest recognition. The proposed neural architecture provides a very good bioactivity classification (F₁ score > 98% on average). Moreover, we devised a suitable Explainable AI (XAI) procedure, which is inspired to the well known Gradient-weighted Class Activation Mapping (Grad-CAM) [19]. Grad-CAM is an explainer used in image classification through Convolutional Neural Networks (CNN) and it generates a heatmap for each class to highlight the parts of an image that contribute to the recognition of that class. At each layer where Grad-CAM is applied, the role of each feature map in explaining the class is weighted using the gradients backpropagated to the layer itself. In [16] a graph based version of Grad-CAM is proposed, and we used this implementation for our molecular explainer that provides a graphical representation highlighting the atoms and/or chemical groups with a key role in the discriminative event. We used the four macro-groups of pharmacophoric features (H-bond donor or acceptor, hydrophobic, aromatic) [6] in this respect.

In general, Grad-CAM is applied only to the last layer of the classifier whose feature maps convey aggregated position-independent information on the features extracted by the deep layers of the network. Rather than providing a global explanation of the classifier behaviour, the key idea behind our approach is trying to explain how the different molecular moieties are involved in predicting a high degree bioactivity. These structures are expected to play a crucial role in binding to the target. As a consequence, we used a hierarchy of explainers placed at different layers to catch information directly at atom, ring, and whole molecule level by leveraging the message passing mechanism that is used in GNNs. The explainer hierarchy for a target is applied purposely to a binary version of our classifier. Such a network has a similar

layer arrangement as the 20-target network, but the layers’ sizes have been designed ad hoc, and a novel training on the selected target has been performed to achieve high accuracy, while avoiding the inherent bias of a multi-target prediction with respect to the different classes. In this paper we present the implementation of the whole explainability procedure for CDK1, which is a well-known regulator of the cell cycle, and has a crucial role in tumor genesis. Our explainability results for nineteen well known drugs that are active on CDK1 were manually validated by expert computational chemists, and this was a very time consuming task. The proposed approach is exactly the same for each target so this choice does not reduce the generality of our results.

2 Methods

All the experiments presented in this work were carried on using a data set which was built by some of the authors [14] and contains small molecules that are active on twenty Kinases. We selected this data set as it was used by a deep neural classifier that leverages the *EMBER* molecular descriptor based on molecular fingerprints. Such a classifier provides state-of-the-art performance both in classification accuracy and Enrichment Factor (EF) values for screening tasks. Even if molecular fingerprints are a well known descriptor, they are not prone to provide explicit information about the single moieties involved in bioactivity, and we started our explainability study from a comparison between fingerprint and graph descriptors. As a consequence, we built a graph version of the twenty target classifier: we expected an increased performance using graphs due to their one-to-one encoding of the chemical information about atoms and bonds, and our prevision was supported by the experimental results. Next, we moved towards a fine explanation of the role of each molecular moiety in the prediction, and the hierarchical explainer was devised in this respect.

2.1 Data preparation

Input molecular graphs for our neural architecture were generated from the canonical SMILES representation. Unlike the other molecular descriptors used in classical approaches for Virtual Screening, molecular graphs account for chemical information both in each atom and its chemical neighborhood. Each node represents an atom as a feature vector, and nine features were selected in the proposed representation:

- Atomic number
- Degree
- Formal Charge
- Hybridization
- Aromaticity
- Total number of hydrogen atoms
- Number of radical electrons
- Information on aromaticity

- Chirality

The set of atom features was later augmented with the 3D coordinates of each atom in active configuration, for the sake of training the single-class architecture used for the hierarchical explainability analysis. These coordinates were calculated by maximising the local minimum of the active conformation for each individual molecule. Edges information concerns the type of bond (double or triple bond) and whether the bond is within a cycle. The size of each molecular graph had several nodes and arcs which vary according to the size of the molecule.

Canonical SMILES were recovered from ChEMBL [1] for all the small molecules whose activity on the target protein is referenced by IC₅₀, K_i, and K_d values. We used a fixed threshold activity value on each target, in order to generate the molecular graphs through the use of the RDKit library, which allows obtaining all the features previously described.

The final dataset consists of 89373 small molecules and has a 1:100 active/inactive ratio for the smallest class that is CLK2. This ratio allows profound assessing of the model generalization abilities as it has more or less the same size of a real world screening task. Training, validation, and test sets were created using a 80%:10%:10% ratio for each target, in order to minimize the comparison bias.

2.2 Graph Convolutional Neural Network

The neural architecture used in this study is made by two main parts: the Graph Convolutional (GC) blocks, and the true classifier which uses dense layers. As reported before, the multi-target, and the single target network share the same arrangement as regards the two parts but with different sizes for each single layer. In the multi-target network, seven GC blocks are employed. Each block consists of a proper GC layer that implements the *1-dimensional Weisfeler-Leman kernel* (1-WL) and has been presented in [15]. Such a layer uses the message-passing algorithm [8] to collect information from the direct neighbors of each node. After the GC layer, each block contains a Rectified Linear Unit (ReLU) activation function and a Layer normalization operation. The primary goal of a GC block is using both the node and the adjacency matrix to collect relevant features from neighboring nodes within the graph.

The message-passing algorithm stacks data coming from neighbours, for each node in the graph. This aggregation process results in an updated set of node features placed along the channel dimension of the data sample. More formally, the algorithm uses a message function M_t and a vertex update function U_t , which is usually implemented as a Multi Layer Perceptron (MLP). Both those functions are learnable and differentiable in order to be trained in a neural network. Given the time-step t , the node v collecting features, the edge e_{vw} connecting node v and any node w in the set $N(v)$ of the neighbors of v in the graph G , and the hidden states h_v^t and h_w^t , the new message m_v at time-step $t + 1$ is calculated as:

$$(1) \quad m_v^{t+1} = \sum_{w \in N(v)} M_t(h_v^t, h_w^t, e_{vw})$$

The new hidden state h_v^{t+1} is then computed using the previous hidden state h_v^t and the new message m_v^{t+1} using the vertex update function:

$$(2) \quad h_v^{t+1} = U_t(h_v^t, m_v^{t+1})$$

For the sake of rich feature extraction, the design the GC layers involved a systematic increase of the number of channels that are progressively doubled in a geometric progression: 32, 64, 128, 256, 512, and 1024. The purpose of this channel augmentation is to yield a more and more meaningful latent representation of the inputs, that is a critical aspect for achieving superior performance in the context of a multi-class classification task involving twenty distinct targets. The augmented node feature vector coming from the graph convolutional operations flows into a Global Average Pooling (GAP) layer. This step is also known as the *readout phase*, and it represents a core operation when using the message-passing algorithm. GAP condenses the information about all the nodes into a one-dimensional vector that averages all the features of the whole graph into a compressed and meaningful vector representation.

The second part of the multi-target network is a neural classifier consisting in four fully connected layers designed for both dimensionality reduction and features manipulation. The original size of 1024 features in the latent representation is reduced sequentially to 512, 256, 64, and 20 channels. ReLU activation functions and dropout layers are also added for each fully connected layer to add non-linearity correlation to the input data. Actual classification is achieved through a sigmoid activation function that rescales the incoming vector into a set of twenty independent probabilities for the input molecule to be active separately on each of the different targets. The whole architecture of the network is reported in 1.

The single target architecture differs significantly from the first one as regards both the number and the size of each layer. It is well known that the global efficacy of a model for Virtual Screening is measured through the ability of correctly prioritizing the *True Positives*, so the main aim of the network is providing a very high sensitivity with respect to the inhibitors of the target that is CDK1 in our experiments. In turn, stressing the network towards high sensitivity performance, makes it able to provide precise explanations about the molecular moieties involved in the inhibition. To achieve this result we operated in two ways: enrichment of the information encoded at each node, and accurate design of the model capacity through a change in the dimensions of the layers. The 3-D coordinates of each atom were computed by maximising the local minimum of the active conformation of the molecule, and they were added to the node features. Moreover, we selected a tighter network than the multi-target one because the task is only a binary classification.

The GC layers in the single target network elaborate the features in a U-Net [17] fashion, first enlarging, and then tightening the channels at each layer until a final 32 features representation is obtained. Seven GC blocks are used where the channels of each GC layer are arranged as follows: 32, 64, 128, 256, 128, 64, and again 32. Layer normalization and ReLU are obviously used in each block. After the GAP, four fully connected layers were used whose channels are respectively 2, 32, 16, and finally 1 that is fed to a sigmoid to estimate the probability for the input to be active on the target. The whole architecture of the single target network is reported in Figure 2 along with an example of the output of the explainers used in the proposed hierarchy.

Both the neural architectures were trained using Weighted Binary Cross-Entropy with a higher weight value for the positives given the strong imbalance between active and inactive classes on targets. In both cases, a grid search was performed to select the hyperparameters properly. The number of GC filters was searched for in the set [1024, 512, 256, 128, 64, 32, 16], learning rates were in the range $[10^{-5}, 10^{-1}]$. The batch size ranged in [8, 64]. Model checkpoint was used to store the best model after each epoch and the early stopping procedure was utilized to determine the ideal number of training epochs. Hyperparameter optimization process took 64 days, and it was carried out on a NVIDIA GeForce RTX 3090 with 10496 CUDA cores.

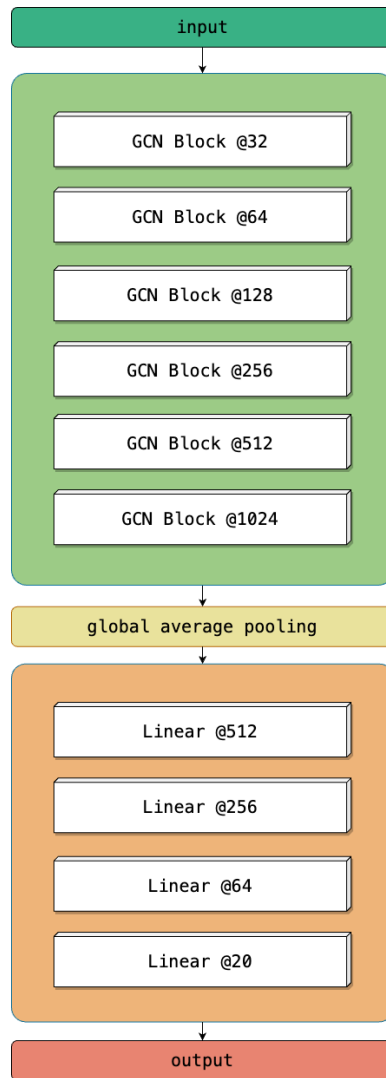


Figure 1: The architecture of the multi-target network

Despite the low architecture complexity, each training session took roughly 8 hours because of the huge computation involved in the GC layers.

2.3 Explainability analysis

As already mentioned, we used XAI techniques to gain information about the most relevant molecular moieties involved in bioactivity prediction; different algorithms were tried in this respect. All the selected XAI approaches belong to the so-called “instance-level methods” i.e. the ones aimed at identifying the input features that contribute mostly to the prediction. At first, we tried GNNExplainer [27], which is a “perturbation-based method” that tracks the change in the output for minor variations of the same input data to determine which features are most important for prediction. GNNExplainer provides a too fine-grained information because it works at feature level, while we were interested to obtain explanations at least at atom (i.e. node) level. As a consequence, we moved towards the class of “gradient and feature-based techniques”. An implementation from the work by Pope et al. [16] was utilized for this purpose. In this work, the authors implemented some graph-based counterparts of three well-established explainability methods, which had been designed originally for convolutional neural networks.

We choose Grad-CAM as the best performing technique in labeling point-wise contributions to positive prediction, at least in the original image domain where pixels are the data units, and the information flows between layers through the convolution operator. In a GC layer, feature maps are built for each node of the graph by message passing (eq. 1). In this way, features at each node encode the information flow from the node neighborhood, and the more deep is the layer the more its features collect information from many message passing steps computed in the previous layers (eq. 2). As a consequence, a feature map at a certain depth d collects information from the d -neighbors of a node.

Grad-CAM aims at visualizing the most active region of the input, when a particular class is predicted. This is done by examining the gradients of the target class score with respect to each feature map in the network layer under investigation. The weight $\alpha_k^{l,c}$, for class c related to the k -th node feature at layer l is computed as:

$$(3) \quad \alpha_k^{l,c} = \frac{1}{N} \sum_{n=1}^N \frac{\partial y^c}{\partial F_{k,n}^l}$$

$F_{k,n}^l$ is the k -th feature value for the single node n in layer l , while y^c is the score for class c obtained from the last network layer, before the output unit. Obviously, the partial derivative term is computed using the chain rule when l is not the last layer. Grad-CAM values for the whole node n are summed over its features, and passed to the ReLU activation function to filter out negative contributions to the prediction of class c .

$$(4) \quad L_{Grad-CAM}[l, n] = \text{ReLU} \left(\sum_k \alpha_k^{l,c} F_{k,n}^l \right)$$

In our implementation $c = 1$ that is we have just a single class score because we implemented our explainer on a binary classifier. Moreover, the ReLU activation function has been removed to capture not only positive contributions to the prediction, but also negative ones. Our choice is motivated by the intrinsic nature of the classification task to be explained. In the image

domain, either single pixels are classified as belonging to a particular class, in the case of semantic segmentation, or the whole image is labelled according to the presence or not of some class discriminative features that are learned by the network. In any case, it is possible to think about classification as a pattern recognition task. As a consequence, the explainer tends to isolate the regions that contributed to the prediction, while discarding the others, and the ReLU activation function is intended for this purpose.

Bioactivity prediction is a classification task where molecules are labelled as positive or negative if they trigger "globally" a particular chemical event or not. Many factors are involved in bioactivity apart from the presence of the classical pharmacophoric structures: molecular chirality, hydrosolubility, use of conformational restriction in the drug design, and so on. All of them can be captured by training the GCNN on a three-dimensional molecular representation with rich information at the nodes, but can not be directly related to just "positive" or "negative" Grad-CAM values at each node. As a consequence we removed ReLU for our explainability task. Moreover, pharmacophoric information is strictly related to the presence in the molecule of particular structures that span atoms' neighborhoods with different size. In view of this consideration we evaluated Grad-CAM multiple times at different depths in the convolutional segment of the network. We used the classical Grad-CAM arrangement after the last layer of the network that is the 7-th one. This explainer is aimed at highlighting relevant features globally, and it is not able to provide information about subtle moieties like acceptors or donors. To reach this aim, we placed also a Grad-CAM explainer at the very first GC layer to consider the atoms' impact in a 1-neighbourhood that is at a bond level. Another explainer was placed after the third layer to catch information related to 3-neighborhoods. At this level, as we analyze the 3-neighborhood of each atom, the action of an entire substructure like aromatic ring or carbonyl ring can be detected.

The whole explanation map has been built as follows. At first, the three Grad-CAM values distribution have been summed for each node:

$$(5) \quad L_{Grad-CAM}[n] = L_{Grad-CAM}[1, n] + L_{Grad-CAM}[3, n] + L_{Grad-CAM}[7, n]$$

The resulting $L_{Grad-CAM}$ distribution has been min-max scaled, and only contributions higher than 0.7 have been regarded as relevant. The RDKit software package has been used to devise pharmacophoric labels for each molecular structure, and the final map reports only relevant contributions colored accordingly to the labels. In particular, H-bond acceptor or donor groups are highlighted in yellow, hydrophobic groups are colored in blue, and the aromatic groups are green. Lastly, atoms without an explicit pharmacophoric label where $L_{Grad-CAM} > 0.7$ are labelled as "relevant", and are colored in red. In Section ?? a detailed analysis is reported about the structures highlighted by our hierarchical Grad-CAM explainer.

3 Results

In this section we present the results for both the multi-target and the CDK1-only classifier, and the explainability analysis is reported for nineteen anti-cancer drugs that are CDK1 inhibitors.

<https://www.rdkit.org/>

Protein	Bal. Accuracy	Sensitivity	F1-Score	AUC
ACK	0.891	0.811	0.979	0.983
ALK	0.929	0.893	0.972	0.987
CDK1	0.921	0.907	0.956	0.969
CDK2	0.932	0.950	0.940	0.971
CDK6	0.916	0.846	0.989	0.988
CHK1	0.923	0.912	0.954	0.977
CK2A1	0.942	0.911	0.979	0.989
CLK2	0.938	0.965	0.929	0.989
DYRK1A	0.913	0.847	0.983	0.986
EGFR	0.930	0.881	0.982	0.990
ERK2	0.927	0.935	0.941	0.977
GSK3B	0.903	0.847	0.970	0.978
INSR	0.893	0.823	0.974	0.977
IRAK4	0.930	0.931	0.953	0.979
ITK	0.928	0.958	0.921	0.981
JKA2	0.945	0.960	0.945	0.984
JNK	0.918	0.946	0.923	0.971
MAP2K1	0.944	0.926	0.969	0.991
MELK	0.916	0.874	0.969	0.982
PDK1	0.913	0.860	0.973	0.986
Avg	0.922	0.904	0.960	0.981

Table 1: Results for 20 target classification

3.1 Multi-class multi-target classification

Results for the 20-target classifier are shown in Table 1 and Table 2. The first table provides the performance metrics of our network as a classifier. The *Balanced Accuracy* assesses the network’s ability to make correct predictions despite the class imbalance, while the *Sensitivity* (also named Recall) focuses solely on the network’s performance in correctly classifying active molecules. The *F1-score* quantifies how well the model can correctly identify positive instances (Recall) while avoiding false positives (Precision). On the other hand, the *Area Under the Curve* (AUC) provides a global measure of the model’s ability to discriminate between positive and negative instances, and it is computed from the curve that plots the Sensitivity vs the False Positive Rate varying the threshold to discriminate positives and negatives.

The second Table reports the measure used to assess the classifier’s ability to prioritize ligands, that is the true outcome of the VS task. The *True Positives vs Positives* ratio (TP/P) is employed to assess correct predictions count relative to the total positives in a given class, the *Enrichment Factor* (EF) metric measures how many times the tested model outperforms a purely random process in predicting a given class. Both these measures are computed for a given topmost percentage of the test set, and we used respectively the 1%, 2%, 5%, and 10% of the whole test set according to the chemical literature.

As already mentioned, we compared the results of the multi-target classifier with another one developed for the same task by some of the authors. In that work molecules were described through a novel molecular embedding that we called EMBER. We carried out this comparison as in our previous work we showed that the EMBER classifier had SOTA performance.

In our results, both the accuracy and sensitivity values indicate that our multi-target network identifies correctly both the positive and negative samples. Particularly, sensitivity in-

creased significantly with respect to the EMBER classifier where it ranged between 0.22 and 0.84. Now, sensitivity has an average value of 0.904, showing that it is much easier for the network to classify positive samples. The comparison between the two networks is summarised in Figure 3 showing the sensitivity for all targets. It is notable that there was a huge improvement in the performance related to sensitivity. Particularly, sensitivity on the CLK2 target raised from 0.22 to 0.938, as it is shown also in Table 1.

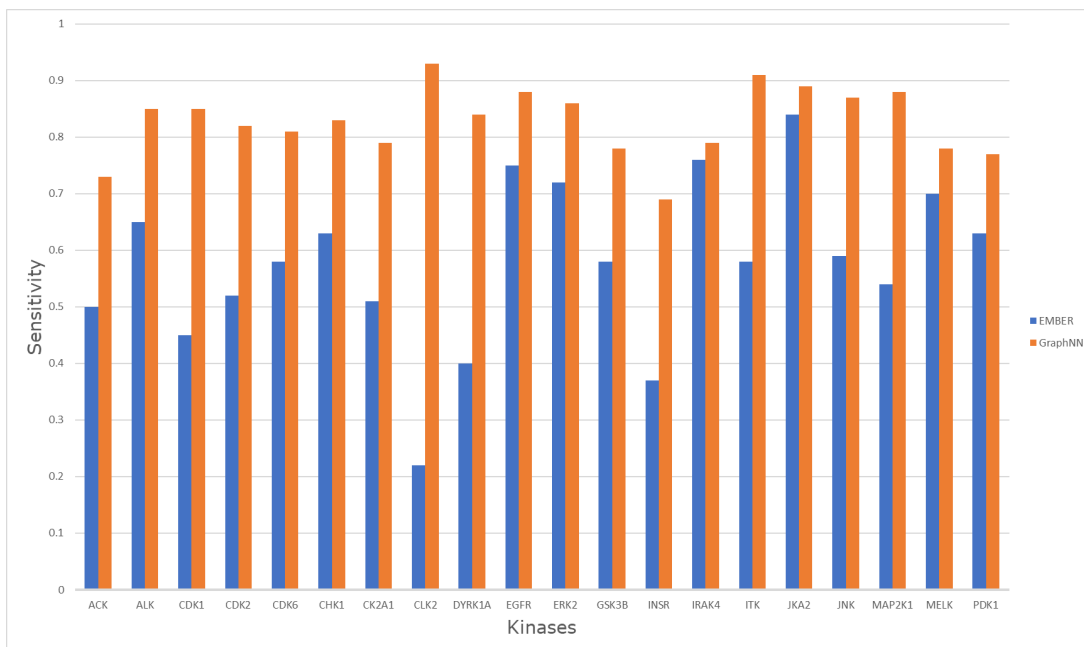


Figure 3: Sensitivity comparison for all the targets between the EMBER and our GC multi-target classifier.

F1-Score values show that the network is able to overcome the dataset imbalance while simultaneously reducing the number of false negatives and false positives. The use of a properly balanced loss made by a weighted cross entropy and a soft F-score worked fine for the classification task. Finally, also the values for TP/P and EF are similar to the ones reported for the EMBER classifier.

3.2 Single-target classification

Classification performance in the CDK1-only network was assessed using the same metrics as described in Section 3.1, and it is shown in Table 3 and 4.

As can be observed, both Balanced Accuracy and Sensitivity are higher than those obtained on the same target in the multi-target classifier, while the performance in terms of both TP/P and EF remained consistent with the ones reported in Table 2.

Protein	TP/P 1%	TP/P 2%	TP/P 5%	TP/P 10%	EF 1%	EF 2%	EF 5%	EF 10%
ACK	72/106	78/106	94/106	100/106	67	36	17	9
ALK	123/254	186/254	227/254	242/254	48	36	17	9
CDK1	80/205	117/205	177/205	190/205	39	28	17	9
CDK2	86/303	141/303	240/303	287/303	28	23	15	9
CDK6	82/104	89/104	94/104	99/104	78	42	18	9
INSR	89/217	123/217	180/217	204/217	41	28	16	9
ITK	98/158	127/158	145/158	154/158	62	40	18	9
JAK2	134/832	268/832	651/832	774/832	16	16	15	9
JNK3	79/105	83/105	93/105	102/105	75	39	17	9
MELK	125/185	158/185	171/185	179/185	67	42	18	9
CHK1	126/343	189/343	269/343	319/343	36	27	15	9
CK2A1	93/151	115/151	128/151	141/151	61	38	16	9
CLK2	52/102	63/102	85/102	96/102	50	30	16	9
DYRK1A	72/174	106/174	144/174	167/174	41	30	16	9
EGFR	129/702	262/702	520/702	641/702	18	18	14	9
ERK2	130/525	260/525	444/525	503/525	24	24	16	9
GSK3	102/393	174/393	293/393	358/393	25	22	14	9
IRAK4	134/339	249/339	311/339	327/339	39	36	18	9
MAP2K1	106/191	133/191	166/191	181/191	55	34	17	9
PDK1	108/187	132/187	164/187	183/187	57	35	17	9

Table 2: TP/P and EF values for 20 target classification

Protein	Bal. Accuracy	Sensitivity	F1-score	AUC
CDK1	0.928	0.954	0.277	0.974

Table 3: Classification performance for the CDK1-only classifier

Protein	TP/P 1%	TP/P 2%	TP/P 5%	TP/P 10%	EF 1%	EF 2%	EF 5%	EF 10%
CDK1	34/109	58/109	109/109	100/109	31.19	26.60	20	9.11

Table 4: prioritization performance for the CDK1-only classifier

3.3 Explainability results

As already detailed in Section 2.3, the main contribution of our work is the hierarchical Grad-CAM graph explainability procedure to devise relevant moieties at different scales in the molecule. Two visual examples of the results provided by our hierarchical graph explainer compared to the docking analysis carried out by an expert in Computational Chemistry are shown in Figure 4 and Figure 5. In such figures, two well known drugs acting as CDK1 inhibitors are reported: the Dinaciclib (PubChem ID: 46926350) and the Meridianin e (PubChem ID: 9995236). The color codes are the one already detailed in Section 2.3.

The explainability procedure was carried out on 19 CDK1 inhibitors, and the results have been compared to either the docking results for the same inhibitors or experimental crystal structures of co-crystallised ligands, when available. The complete visual results for all the drugs are reported in the Supplementary Materials. Our methodology is consistent with what was observed using experimental structures in 17 of 19 known drugs, and they are reported

in Table ?? which lists the generic name of the drug, the PubChem ID, a binary assessment made by the expert on the goodness of prediction of the molecular features involved in the host-guest interaction between drug and target that we called *Guest Feature Prediction* (GFP) and the detailed accordance of the moieties coloring to the docking outcomes. Here, the expert verified if each piece of information gathered from the docking had been colored properly by our explainer that is with a label in accordance with the docking procedure. We reported such information in terms of single statements that have been red colored in case the explainer missed the correct label.

We performed also an ablation study to confirm our intuitions on the explainer procedure that is the need of a hierarchy of explainers acting at different neighborhood size, and the removal of the ReLU function in each Grad-CAM explainer to take into account also negative contributions to the inhibitory action of the ligand under investigation. The results are reported in Table ??, and they show clearly that the number of missed labels increases significantly both when we use a single layer explainer and if we leave the ReLU in the Grad-CAM output. Figure 6 reports the outputs provided by each layer in the hierarchy for the Dinaciclib. Interestingly, every layer of the explainer provides an important contribution to the final molecular interpretation. Indeed, the figure shows that the layer 3 explainer (the one considering the 3-neighborhood of each atom) is capable to catch important features as the H-bond donor N6, that are useful for the ligand protein complex stabilisation. Such a crucial information is then lost in the layer 7 explainer where molecular substructures are considered. On the other hand, the highest level of molecular interpretation is crucial to catch all the aromatic and lipophilic moieties that could be lost in the lower levels of the hierarchy.

4 Discussion

In view of the presented results, our explainer could be considered as a guidance, together with classical structure-based methods, to analyze crucial molecular moieties involved in the successful binding to a specific target. We showed that our multi-target GC classifier outperforms the EMBER classifier, proposed by some of the authors, for target assignment. It is well known, in fact, that molecular fingerprints can suffer for the correct interpretation of molecular moieties, especially for large and diverse chemical spaces datasets [25]. The combined use of different levels of molecular embeddings seems to be more and more efficient in catching crucial molecular features for assigning the target. The main strength of the presented approach is the combination of different explanation layers (from single atoms to complex structures). Every layer is capable to catch different aspects of a molecule, and every step enriches the others giving a complete interpretation of both the molecule and the moieties useful to interact with a specific target. As it is demonstrated in Figure 6 for Dinaciclib, all the layers complement each other in a crucial way to avoid losing chemical information. When going into more detail, it is clear that the proposed model is capable to rationally explain ligand moieties involved in the stabilisation of the host-guest interaction. For the majority of the investigated ligands (17 out of 19), our method was in accordance with the observations resulting from the use of either protein-ligand complexes from experimental crystals or docking algorithms (when crystals were not available). When the message passing mechanism at the topmost level is regarded, the entire structure is considered, accounting for ‘regions’ that actively contribute to the classification. Considering the whole structure of the molecules instead of single atoms or small patterns, provides insights about the important roles of the molecules to reach the target and bind to it

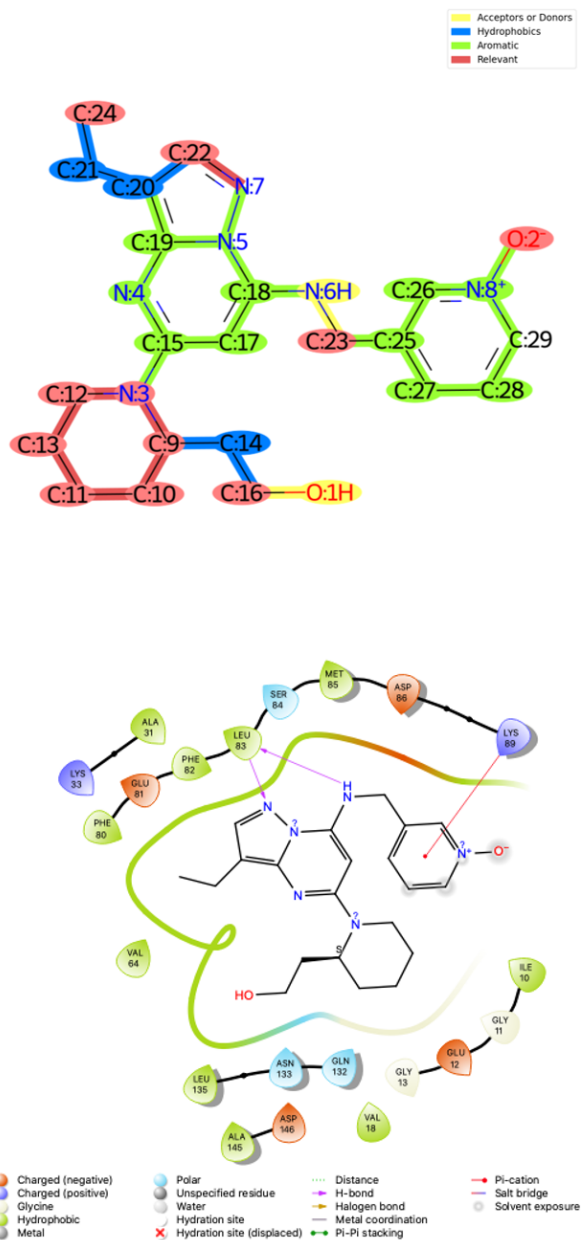


Figure 4: Comparison of the results obtained using our hierarchical explainer versus molecular docking for Dinaciclib.

strongly. For two compounds analysed, the proposed explainer did not found relevant chemical parts to bind the CDK1 receptor. Given the nature of the DL techniques used in this work, it

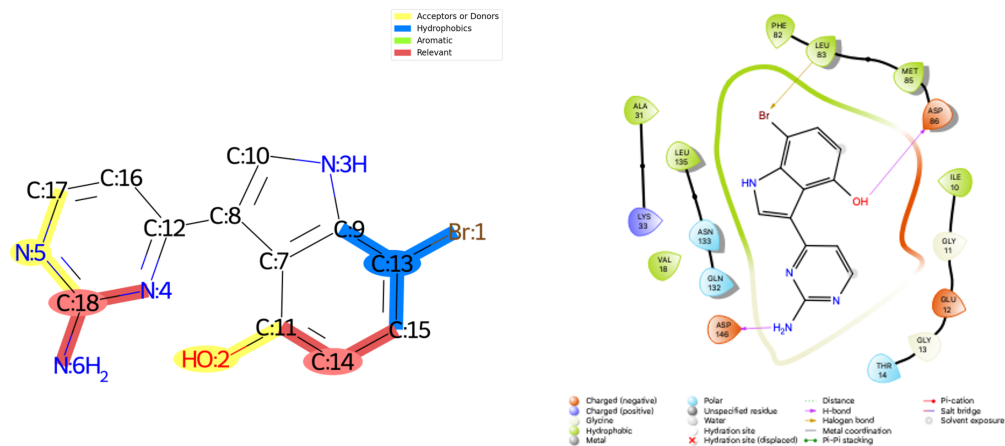


Figure 5: Comparison of the results obtained using our hierarchical explainer versus molecular docking for Meridianin e.

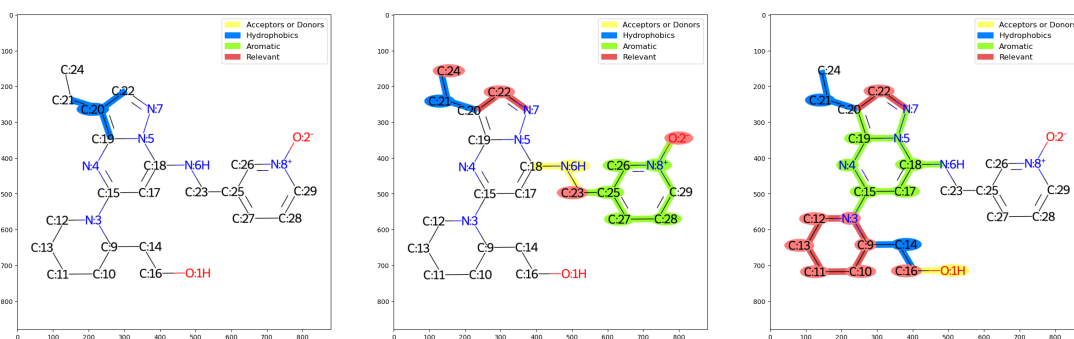


Figure 6: Visualisation of the results provided by each single layer in our explainer Dinaciclib (PubChem CID: 46926350). left: layer 1, center: layer 3, right: layer 7

is not possible to devise exactly the reason of the model's failure for these molecules. For sure, the chemical structures of Flavopiridol and RGB286638 differ from the other molecules in the training set where the H-bonds are mainly driven by nitrogen instead of oxygen. Indeed, one can think that the molecular complexity of RGB286638 puts this ligand out of the applicability domain of the training and test set. For this reason, our model could fail in detecting some functional parts of the molecule as the interacting core. Similarly, Flavopiridol, a flavonoids derivative, has a non common structure when compared to those in the initial dataset, while maintaining the H-bond acceptor/donor pattern useful for CDK1 binding.

Drug	Pubchem ID	GFP	Accordance to docking
Flavopiridol	5287969	no	Hydrogen bond N:7 – ASP146; Pi-cation N:7 – TYR15; Hydrogen bond O:5H – GLU81; Hydrogen bond O:6 – LEU83;
Roscovitine	160355	yes	Hydrogen bond O:1H – ASN133; Hydrogen bond N:3H – LEU83; Pi-Pi interaction – LYS89;
RO3306	136240579	yes	Hydrogen bonds N:4H – O:3 – LEU83; Pi-Pi interaction – LYS89;
Dinaciclib	46926350	yes	Hydrogen bonds N:5 – N:6H – LEU83; Pi-Pi interaction – LYS89;
Milciclib	16718576	yes	Pi-Pi interaction – LYS89; Hydrogen bond O:1 – LYS33
Palbociclib	5330286	yes	Pi-Pi interaction – LYS89; Hydrogen bond N:8H – ASP86; Hydrogen bond O:2 – LYS33
Meriolin	24801699	yes	Hydrogen bond N:6H2 – ASP146; Hydrogen bond N:3H – LEU83
Variolin	9817550	yes	Hydrogen bonds N:3H – N:5H2 – LEU83; Hydrogen bond N:8H2 – ASP146;
Meridianin	9995236	yes	Hydrogen bond O:2H – ASP86; Halogen bond Br:1 – LEU83;
AZD5438	16747683	yes	Hydrogen bonds N:7H – N:8 – LEU83; Hydrogen bond O:2 or O:3 – ASP86
Roniciclib	45380979	yes	Hydrogen bond O:7H – LYS33; Hydrogen bonds N:9H – N:10 – LEU83; Hydrogen bond O:7H – LYS33;
SNS-032	3025986	yes	Hydrogen bonds N:8 – N:6H – LEU83; Hydrogen bond N:7 – LYS33;
Fostamatinib	11671467	yes	Pi-Pi interaction – LYS89; Hydrogen bond O:6H – O:7H – O:4 – LYS33;
AG-024322	135413565	yes	Hydrogen bond N:5 – LYS89; Hydrogen bond N:3H – SER84; Hydrogen bond N:4H – ASP89;
R547	6918852	yes	Hydrogen bond N:9H – ASP89; Hydrogen bond O:6 – LYS33;
RGB-286638	11285001	no	Hydrogen bond N:8 – LYS89; Hydrogen bond O:2 – GLN132; Hydrogen bond O:1 – LYS9;
ZK304709	59733314	yes	Pi-Pi interaction – LYS89; Hydrogen bond N:7H – GLU12; Hydrogen bond N:6 – GLU8;
JNJ-7706621	5330790	yes	Hydrogen bond N:12H2 – GLU81; Hydrogen bonds N:10 – N:7H – LEU83;
C26H31N7O*	46916588	yes	Pi-Pi interaction – LYS89; Hydrogen bonds N:7 – N:6H – LEU83;

*Molecular formula of 2-[(2S)-1-[8-ethyl-4-[(4-pyridin-2-ylphenyl)methylamino]pyrazolo[1,5-a][1,3,5]triazin-2-yl]piperidin-2-yl]ethanol

Table 5: Results of the comparison between our explainer and the results of the docking analysis for the 19 drugs tested. Black text depicts the interactions predicted in accordance with molecular docking, while red text indicates divergence

Drug	Level 3	Level 7	Accordance to docking w/ ReLU	Our results (w/o ReLU)
Flavopiridol	H-bond N:7 – ASP146; Pi-cation N:7 – TYR15; H-bond O:5H – GLU81; H-bond O:6 – LEU83;	H-bond N:7 – ASP146; Pi-cation N:7 – TYR15; H-bond O:5H – GLU81; H-bond O:6 – LEU83;	H-bond N:7 – ASP146; Pi-cation N:7 – TYR15; H-bond O:5H – GLU81; H-bond O:6 – LEU83;	H-bond N:7 – ASP146; Pi-cation N:7 – TYR15; H-bond O:5H – GLU81; H-bond O:6 – LEU83;
Roscovitine	H-bond O:1H – ASN133; H-bond N:3H – LEU83; Pi-Pi – LYS89;	H-bond O:1H – ASN133; H-bond N:3H – LEU83; Pi-Pi – LYS89;	H-bond O:1H – ASN133; H-bond N:3H – LEU83; Pi-Pi – LYS89;	H-bond O:1H – ASN133; H-bond N:3H – LEU83; Pi-Pi – LYS89;
RO3306	H-bonds N:4H – O:3 – LEU83; Pi-Pi – LYS89;	H-bonds N:4H – O:3 – LEU83; Pi-Pi – LYS89;	H-bonds N:4H – O:3 – LEU83; Pi-Pi – LYS89;	H-bonds N:4H – O:3 – LEU83; Pi-Pi – LYS89;
Dinaciclib	H-bonds N:5 – N:6H – LEU83; Pi-Pi – LYS89;	H-bonds N:5 – N:6H – LEU83; Pi-Pi – LYS89;	H-bonds N:5 – N:6H – LEU83; Pi-Pi – LYS89;	H-bonds N:5 – N:6H – LEU83; Pi-Pi – LYS89;
Miliciclib	Pi-Pi – LYS89; H-bond O:1 – LYS33;	Pi-Pi – LYS89; H-bond O:1 – LYS33;	Pi-Pi – LYS89; H-bond O:1 – LYS33;	Pi-Pi – LYS89; H-bond O:1 – LYS33;
Palbociclib	Pi-Pi – LYS89; H-bond N:8H – ASP86; H-bond O:2 – LYS33;	Pi-Pi – LYS89; H-bond N:8H – ASP86; H-bond O:2 – LYS33;	Pi-Pi – LYS89; H-bond N:8H – ASP86; H-bond O:2 – LYS33;	Pi-Pi – LYS89; H-bond N:8H – ASP86; H-bond O:2 – LYS33;
Meriolin	H-bond N:6H2 – ASP146; H-bond N:3H – LEU83;	H-bond N:6H2; H-bond N:3H – LEU83;	H-bond N:6H2; H-bond N:3H – LEU83;	H-bond N:6H2; H-bond N:3H – LEU83;
Variolin	H-bonds N:3H – N:5H2 – LEU83; H-bond N:8H2 – ASP146;	H-bonds N:3H – N:5H2 – LEU83; H-bond N:8H2 – ASP146;	H-bonds N:3H – N:5H2 – LEU83; H-bond N:8H2 – ASP146;	H-bonds N:3H – N:5H2 – LEU83; H-bond N:8H2 – ASP146;
Meridianin	H-bond O:2H – ASP86; Halogen bond Br:1 – LEU83;	H-bond O:2H – ASP86; Halogen bond Br:1 – LEU83;	H-bond O:2H – ASP86; Halogen bond Br:1 – LEU83;	H-bond O:2H – ASP86; Halogen bond Br:1 – LEU83;
AZD5438	H-bonds N:7H – N:8 – LEU83; H-bond O:2 or O:3 – ASP86	H-bonds N:7H – N:8 – LEU83; H-bond O:2 or O:3 – ASP86	H-bonds N:7H – N:8 – LEU83; H-bond O:2 or O:3 – ASP86	H-bonds N:7H – N:8 – LEU83; H-bond O:2 or O:3 – ASP86
Roniciclib	H-bond O:7H – LYS33; H-bonds N:9H – N:10 – LEU83;	H-bond O:7H – LYS33; H-bonds N:9H – N:10 – LEU83;	H-bond O:7H – LYS33; H-bonds N:9H – N:10 – LEU83;	H-bond O:7H – LYS33; H-bonds N:9H – N:10 – LEU83;
SNS-032	H-bonds N:8 – N:6H – LEU83; H-bond N:7 – LYS33;	H-bonds N:8 – N:6H – LEU83; H-bond N:7 – LYS33;	H-bonds N:8 – N:6H – LEU83; H-bond N:7 – LYS33;	H-bonds N:8 – N:6H – LEU83; H-bond N:7 – LYS33;
Postamatinib	Pi-Pi – LYS89; H-bond O:6H – O:7H – O:4 – LYS33;	Pi-Pi – LYS89; H-bond O:6H – O:7H – O:4 – LYS33;	Pi-Pi – LYS89; H-bond O:6H – O:7H – O:4 – LYS33;	Pi-Pi – LYS89; H-bond O:6H – O:7H – O:4 – LYS33;
AG-024322	H-bond N:5 – LYS89; H-bond N:3H – SER84; H-bond N:4H – ASP89;	H-bond N:5 – LYS89; H-bond N:3H – SER84; H-bond N:4H – ASP89;	H-bond N:5 – LYS89; H-bond N:3H – SER84; H-bond N:4H – ASP89;	H-bond N:5 – LYS89; H-bond N:3H – SER84; H-bond N:4H – ASP89;
R547	H-bond N:9H – ASP89; H-bond O:6 – LYS33;	H-bond N:9H – ASP89; H-bond O:6 – LYS33;	H-bond N:9H – ASP89; H-bond O:6 – LYS33;	H-bond N:9H – ASP89; H-bond O:6 – LYS33;
RGB-286638	H-bond N:8 – LYS89; H-bond O:2 – GLN132; H-bond O:1 – LYS9;	H-bond N:8 – LYS89; H-bond O:2 – GLN132; H-bond O:1 – LYS9;	H-bond N:8 – LYS89; H-bond O:2 – GLN132; H-bond O:1 – LYS9;	H-bond N:8 – LYS89; H-bond O:2 – GLN132; H-bond O:1 – LYS9;
ZK304709	Pi-Pi – LYS89; H-bond N:7H – GLU12; H-bond N:6 – GLU8;	Pi-Pi – LYS89; H-bond N:7H – GLU12; H-bond N:6 – GLU8;	Pi-Pi – LYS89; H-bond N:7H – GLU12; H-bond N:6 – GLU8;	Pi-Pi – LYS89; H-bond N:7H – GLU12; H-bond N:6 – GLU8;
JNJ-7706621	H-bond N:12H2 – GLU81; H-bonds N:10 – N:7H – LEU83;	H-bond N:12H2 – GLU81; H-bonds N:10 – N:7H – LEU83;	H-bond N:12H2 – GLU81; H-bonds N:10 – N:7H – LEU83;	H-bond N:12H2 – GLU81; H-bonds N:10 – N:7H – LEU83;
C26H31N7O**	Pi-Pi – LYS89; H-bonds N:7 – N:6H – LEU83;	Pi-Pi – LYS89; H-bonds N:7 – N:6H – LEU83;	Pi-Pi – LYS89; H-bonds N:7 – N:6H – LEU83;	Pi-Pi – LYS89; H-bonds N:7 – N:6H – LEU83;

*Molecular formula of 2-[(2S)-1-[8-ethyl-4-[(4-pyridin-2-ylphenyl)methylamino]pyrazolo[1,5-a][1,3,5]triazin-2-yl]piperidin-2-yl]ethanol

Table 6: Ablation study results. The accordance to docking is reported using the layer 3 explainer alone, the layer 7 explainer alone, and the full hierarchical explainer with ReLU respectively, for each of the 19 drugs tested. The fourth column reports our results. In black are shown the interactions predicted in accordance with molecular docking and in red the divergences.

5 Conclusion

The use of AI in chemoinformatics allowed the rise of ligand-based methods that were outclassed by structure-based methods in the last years. Structure-based methods offer the possibility to look deeper in the binding site of a protein allowing scientists to predict how ligand could bind to a specific target. Anyway, It is well known that the use of structure-based methods in drug design could be strongly affected by the protein and ligand conformation in retrieving important protein-ligand interactions. Moreover, high quality protein-ligand complexes are not always available in public databases. In our work, a novel mixed ligand/structure-based VS approach has been presented in this work, which exploits structural information using a

novel eXplainable AI (XAI) procedure on a Deep Neural Network trained for a ligand-based VS task. The presented explainer leverages the algorithmic characteristics of the well-known Grad-CAM explainer for Graph Convolutional Neural Networks based on message passing. Moving from the SOTA results obtained in ligand-based VS with a multi-target classifier which uses the EMBER molecular descriptor, we built a novel classifier relying on GCNNs applied to molecular graphs. Such a multi-target classifier outperformed our previous result, and formed the trained backbone for our explainability analysis. The main idea is using a hierarchy of Grad-CAM explainers placed at different layers of the network where the message passing takes into account a wider and wider neighborhood of each atom. The explanations at each level are then summed together to provide a global map where the different molecular moieties involved in the bioactivity prediction are highlighted and labelled with their role using the well known RDKit package. In our implementation, we applied the explainer to a single target version of the classifier to avoid the inherent classification bias arising in multi-class architectures. We built a CDK1-only classifier that was tuned properly, and the explainability results on 19 well known drugs with CDK1 inhibitory action were tested by a Computational Chemistry expert. The results are very good: 17 of 19 explanations are in accordance with the docking analysis carried out by the expert.

Differently from pure structure-based methods, the results obtained from our method enlighten not only the interacting partners but also the molecular moieties involved, for example, in the hydrophobic interactions (useful for entropy driven binding) and other chemical parts responsible for the recognition of the target. The main strength of our method is the use of combined explainability layers that taken together are capable to account for both the whole molecular structure and functional groups connections. As a result of this architecture, it is possible to correctly assign a target to each molecule and retrieve the main molecule moieties involved in the target assignation/binding. Such a result is not retrievable in other computational techniques used for Virtual Screening, letting our method to unveil hidden molecular moieties useful for binding a specific target. Our methods The explainability approach herein presented, will be applied to other targets, and the molecules prioritised by the multi-target classifier will be tested on a panel of kinases in order to experimentally validate the approach.

Supplementary information

A detailed description of the predictive results obtained from our hierarchical explainer for 19 approved CDK1 drugs is provided in the attached file "supplementary_material.pdf".

Abbreviations

- CADD. Computer-Aided Drug Design
- VS. Virtual Screening
- SAR. Structure Activity Relationship
- XAI. Explainable AI
- EMBER. EMBedding multipLE molecular fingeRprints
- IC50. Half Maximal Inhibitory Concentration

- Ki. Inhibition constant
- Kd. Dissociation constant
- MLP. Multi Layer Perceptron
- PDB. Protein Data Bank
- ReLU. Rectified Linear Unit
- wBCE. Weighted Binary Cross-Entropy
- Grad-CAM. Gradient-weighted Class Activation Mapping
- TP. True Positive
- P. Positive
- TN. True Negative
- N. Negative
- TP/P. True Positive vs Positive ratio
- EF. Enrichment Factor

References

- [1] ChEMBL Database. <https://www.ebi.ac.uk/chembl/>. Accessed: 24/09/2018.
- [2] Azizeh Abdolmaleki, Jahan B. Ghasemi, and Fatemeh Ghasemi. Computer aided drug design for multi-target drug design: Sar /qsar, molecular docking and pharmacophore methods. *Current Drug Targets*, 18(5):556–575, April 2017.
- [3] Meriem Bahi and Mohamed Batouche. Deep learning for ligand-based virtual screening in drug discovery. In *2018 3rd International Conference on Pattern Analysis and Intelligent Systems (PAIS)*, pages 1–5, 2018.
- [4] Kristy A Carpenter, David S Cohen, Juliet T Jarrell, and Xudong Huang. Deep learning and virtual drug screening. *Future Medicinal Chemistry*, 10(21):2557–2567, 2018. PMID: 30288997.
- [5] Xin Chen, Xien Liu, and Ji Wu. Drug-drug interaction prediction with graph representation learning. In *2019 IEEE International Conference on Bioinformatics and Biomedicine (BIBM)*, page 354–361, November 2019.
- [6] Pitchai Daisy, Sanjeev Kumar Singh, Periyasamy Vijayalakshmi, Chandrabose Selvaraj, Manikkam Rajalakshmi, and Sukumaran Suveena. A database for the predicted pharmacophoric features of medicinal compounds. *Bioinformatics*, 6(4):167–168, May 2011.
- [7] Alexej Dick and Simon Cocklin. Bioisosteric replacement as a tool in anti-hiv drug design. *Pharmaceuticals*, 13(33):36, March 2020.

- [8] Justin Gilmer, Samuel S Schoenholz, Patrick F Riley, Oriol Vinyals, and George E Dahl. Neural message passing for quantum chemistry. In *International conference on machine learning*, pages 1263–1272. PMLR, 2017.
- [9] Steven Kearnes, Kevin McCloskey, Marc Berndl, Vijay Pande, and Patrick Riley. Molecular graph convolutions: moving beyond fingerprints. *Journal of Computer-Aided Molecular Design*, 30(8):595–608, August 2016.
- [10] György M. Keserü and Gergely M. Makara. Hit discovery and hit-to-lead approaches. *Drug Discovery Today*, 11(15):741–748, August 2006.
- [11] Talia B. Kimber, Yonghui Chen, and Andrea Volkamer. Deep learning in virtual screening: Recent applications and developments. *International Journal of Molecular Sciences*, 22(9):4435, April 2021.
- [12] Thomas N Kipf and Max Welling. Semi-supervised classification with graph convolutional networks. *arXiv preprint arXiv:1609.02907*, 2016.
- [13] Fang-Yu Lin and Alexander D. MacKerell. *Force Fields for Small Molecules*, volume 2022 of *Methods in Molecular Biology*, page 21–54. Springer New York, New York, NY, 2019.
- [14] Isabella Mendolia, Salvatore Contino, Giada De Simone, Ugo Perricone, and Roberto Pirrone. Ember—embedding multiple molecular fingerprints for virtual screening. *International Journal of Molecular Sciences*, 23(44):2156, Jan 2022.
- [15] Christopher Morris, Martin Ritzert, Matthias Fey, William L Hamilton, Jan Eric Lenssen, Gaurav Rattan, and Martin Grohe. Weisfeiler and leman go neural: Higher-order graph neural networks. In *Proceedings of the AAAI conference on artificial intelligence*, volume 33, pages 4602–4609, 2019.
- [16] Phillip E. Pope, Soheil Kolouri, Mohammad Rostami, Charles E. Martin, and Heiko Hoffmann. Explainability methods for graph convolutional neural networks. *2019 IEEE/CVF Conference on Computer Vision and Pattern Recognition (CVPR)*, pages 10764–10773, 2019.
- [17] Olaf Ronneberger, Philipp Fischer, and Thomas Brox. U-net: Convolutional networks for biomedical image segmentation. In *Medical Image Computing and Computer-Assisted Intervention—MICCAI 2015: 18th International Conference, Munich, Germany, October 5–9, 2015, Proceedings, Part III 18*, pages 234–241. Springer, 2015.
- [18] Franco Scarselli, Marco Gori, Ah Chung Tsoi, Markus Hagenbuchner, and Gabriele Monfardini. The graph neural network model. *IEEE Transactions on Neural Networks*, 20(1):61–80, 2009.
- [19] Ramprasaath R. Selvaraju, Michael Cogswell, Abhishek Das, Ramakrishna Vedantam, Devi Parikh, and Dhruv Batra. Grad-cam: Visual explanations from deep networks via gradient-based localization. *International Journal of Computer Vision*, 128(2):336–359, Feb 2020. arXiv:1610.02391 [cs].

- [20] Jonathan M. Stokes, Kevin Yang, Kyle Swanson, Wengong Jin, Andres Cubillos-Ruiz, Nina M. Donghia, Craig R. MacNair, Shawn French, Lindsey A. Carfrae, Zohar Bloom-Ackermann, Victoria M. Tran, Anush Chiappino-Pepe, Ahmed H. Badran, Ian W. Andrews, Emma J. Chory, George M. Church, Eric D. Brown, Tommi S. Jaakkola, Regina Barzilay, and James J. Collins. A deep learning approach to antibiotic discovery. *Cell*, 180(4):688–702.e13, 2020.
- [21] Shan Sun and David J. Huggins. Assessing the effect of forcefield parameter sets on the accuracy of relative binding free energy calculations. *Frontiers in Molecular Biosciences*, 9:972162, September 2022.
- [22] Thomas Unterthiner, Andreas Mayr, and Jörg Kurt Wegner. Deep learning as an opportunity in virtual screening. 2015.
- [23] Shudong Wang, Zhenzhen Du, Mao Ding, Alfonso Rodriguez-Paton, and Tao Song. Kg-dti: a knowledge graph based deep learning method for drug-target interaction predictions and alzheimer’s disease drug repositions. *Applied Intelligence*, 52(1):846–857, January 2022.
- [24] Zhenqin Wu, Bharath Ramsundar, Evan N Feinberg, Joseph Gomes, Caleb Geniesse, Aneesh S Pappu, Karl Leswing, and Vijay Pande. Moleculenet: a benchmark for molecular machine learning. *Chemical science*, 9(2):513–530, 2018.
- [25] Jingbo Yang, Yiyang Cai, Kairui Zhao, Hongbo Xie, and Xiujie Chen. Concepts and applications of chemical fingerprint for hit and lead screening. *Drug Discovery Today*, 27(11):103356, 2022.
- [26] Kevin Yang, Kyle Swanson, Wengong Jin, Connor Coley, Philipp Eiden, Hua Gao, Angel Guzman-Perez, Timothy Hopper, Brian Kelley, Miriam Mathea, Andrew Palmer, Volker Settels, Tommi Jaakkola, Klavs Jensen, and Regina Barzilay. Analyzing learned molecular representations for property prediction. *Journal of Chemical Information and Modeling*, 59(8):3370–3388, 2019. PMID: 31361484.
- [27] Zhitao Ying, Dylan Bourgeois, Jiaxuan You, Marinka Zitnik, and Jure Leskovec. Gnnexplainer: Generating explanations for graph neural networks. *Advances in neural information processing systems*, 32, 2019.
- [28] Xiangxiang Zeng, Xinqi Tu, Yuansheng Liu, Xiangzheng Fu, and Yansen Su. Toward better drug discovery with knowledge graph. 72:114–126, February 2022.
- [29] Jie Zhou, Ganqu Cui, Shengding Hu, Zhengyan Zhang, Cheng Yang, Zhiyuan Liu, Lifeng Wang, Changcheng Li, and Maosong Sun. Graph neural networks: A review of methods and applications. *AI Open*, 1:57–81, 2020.